IEEE Access
Multidisciplinary | Rapid Review | Open Access Journal

Received October 23, 2020, accepted November 3, 2020, date of publication November 26, 2020,
date of current version December 14, 2020.

Digital Object Identifier 10.1109/ACCESS.2020.3040711

Nonlinear Magnon Scattering Mechanism for Microwave Pumping in Magnetic Films

TAO QU[1,2], (Member, IEEE), ANEESH VENUGOPAL[1], (Graduate Student Member, IEEE), JAMES M. ETHERIDGE[2], WILLIAM K. PERIA[2], KARTHIK SRINIVASAN[1], (Graduate Student Member, IEEE), BETHANIE J. H. STADLER[1], (Senior Member, IEEE), PAUL A. CROWELL[2], (Member, IEEE), AND R. H. VICTORA[1], (Fellow, IEEE)

[1]Department of Electrical and Computer Engineering, University of Minnesota, Minneapolis, MN 55455, USA
[2]School of Physics and Astronomy, University of Minnesota, Minneapolis, MN 55455, USA

Corresponding author: R. H. Victora (victo004@umn.edu)

This work was supported in part by DARPA M3IC Program under Grant W911NF-17-1-0100, in part by the Center for Micromagnetics and Information Technologies (MINT), in part by SMART, in part by SRC NCore Center sponsored by NIST, in part by NSF through the Extreme Science and Engineering Discovery Environment (XSEDE) under Grant ACI-1548562.

ABSTRACT Magnon scattering enables non-linear microwave devices, such as frequency selective limiters and signal to noise enhancers. It may also impact information transfer within spintronic devices. Here, a quantitative understanding of magnon processes in thin films is developed using micromagnetic simulations, in combination with newly developed analytic theory and experimental data. A technique for calculating the number of magnons at each frequency and wavevector as a function of external input such as power and frequency is identified. It is shown that, near the nonlinear threshold, the dominant parametrically excited magnon pairs are those with minimal group velocity and the correct energy. These results complement Brillouin Light Scattering experiments and indicate a path for wavevector-modulated magnon production based only on simulated results and/or analytic theory, a desirable goal for information transfer and communication.

INDEX TERMS Magnetic films, micromagnetics, magnonics, microwave magnetics, nonlinear microwave absorption.

I. INTRODUCTION

The nonlinear properties of magnons, quasi-particles describing the collective excitation of spins, have recently become a focus of research for both their applications to radio frequency(RF) and to spintronic devices. Magnetic thin films, especially those composed of low dissipation materials, provide an accessible system for the study of nonlinear processes. Three major classes of nonlinear processes are chaotic dynamics [1], [2], soliton excitation and propagation [3], and microwave-pump-induced magnon processes [4]–[6], often referred to as Suhl instabilities [7]. Microwave-pumping-induced magnon processes, which are the focus of this article, are highly tunable [8] and can be well-controlled [9], [10]. A common technique to excite the magnons is high power microwave pumping at ferromagnetic resonance [11]–[15]. When the microwave power exceeds a well-defined threshold, the response of the system is nonlinear. In this nonlinear regime, scattering happens among multiple magnon modes [11]–[13].

In recent studies of nonlinear magnon scattering, the scattering models [16] are mostly simplified, which yield incomplete knowledge of the dominant magnon modes, such as the wavevectors and populations. The original Suhl theory [7] for multimagnon scattering is for a spheroid, in which symmetry of the two transverse directions to the bias field is present. In the more typical (and useful) case of a thin film, the associated anisotropy between the in-plane and out-of-plane transverse directions leads to symmetry breaking, an increased role for magnetostatic interactions, and greater distortion of the magnons. Some interesting previous work for films focused on 4-magnon scattering [5] or off-resonance pumping [4], [6], however, a more rigorous treatment of the three-magnon-scattering process at on-resonance

The associate editor coordinating the review of this manuscript and approving it for publication was Guijun Li.

pumping remains to be seen. Brillouin Light Scattering [17], [18] observes magnons for powers well above the nonlinear threshold where there is sufficient optical sensitivity: scattering much closer to the threshold is expected to produce magnons concentrated in a small region of wavevectors that may be useful for applications. This all suggests a need for a quantitatively accurate description of the magnon scattering process, through numerical calculations, that could provide explicit information in a wider dynamic range. Such a description can help gain insights into connections between multiple physical considerations, such as magnon dispersion, group velocity and wavevectors. However, these calculations are large-scale in both spatial and temporal domain, and so far have not been performed.

Nonlinear magnon-based behavior is of great interest, partly because important RF devices rely on such behavior in order to realize their functionalities. One such example is that of RF devices in telecommunication/radar systems [19]–[21], e.g. signal to noise ratio enhancers (SNEs) and frequency selective limiters (FSLs). Proper use of the nonlinear behavior can exclude interference and noise outside prescribed frequency bands, or even cut off excessively large signals at the same frequencies as the signal of interest. These devices consume much lower power and are much simpler to implement than their electrical counterparts. However, significant challenges exist in the miniaturization of these devices, due to the lack of proper design rules that depend on proper treatment of the nonlinear magnons.

On the other hand, there are also devices where nonlinear magnons lead to undesirable effects, e.g., novel spintronic devices that are proposed to be used in computing systems [22], such as logic gates. It has been noticed recently that nonlinear magnons can increase the noise level of the system [23]: at high power beyond a power threshold, the noise increases sharply. This increased noise level limits the device's efficiency. However, the connection between the noise and the nonlinear magnons is not explicitly understood, which limits the ability to reduce such noise. The following study should therefore be highly beneficial towards predictive design and optimization of such devices.

In this article, we provide accurate descriptions of the magnon scattering process through numerical simulation. Using these calculations, we explicitly count the magnon number at each frequency and wavevector as a function of external input in Sec. III, which explicitly identifies the dominant magnons in the scattering process. We perform both experimental homodyne spectroscopy of ferromagnetic resonance and numerical calculations in a wide dynamic range in Sec. IV, whose consistency is a benchmark verifying the accuracy of calculations. Furthermore, we identify the exact magnon pairs that are generated as the power first crosses the threshold for non-linear magnon scattering, and uncover the connection between the magnon pairs and the group velocity in Sec. V.

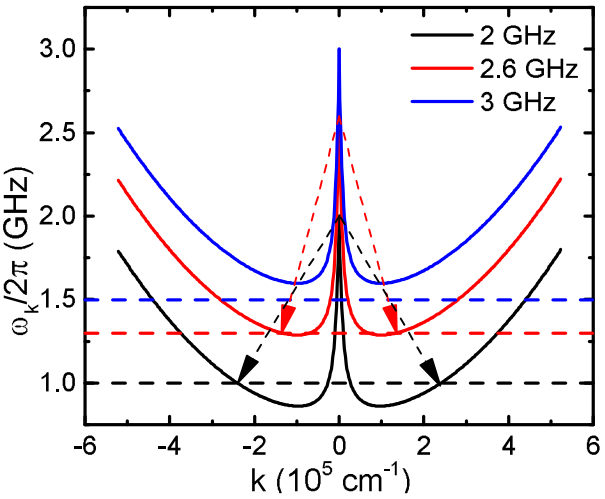

FIGURE 1. The magnon scattering mechanism at resonance for various microwave frequencies. The wavevector $\tilde{k}$ in the dispersion is parallel to $\tilde{H}$. At 2 GHz and 2.6 GHz (black and red curves), k ≠0 modes exist satisfying $\omega_{\mathbf{k}} = \omega_p/2$ and magnon scattering is possible. In contrast, at 3 GHz (blue curve), there are no modes satisfying $\omega_k = \omega_p/2$, and magnon scattering is suppressed. The dashed color lines are at $\omega_p/2$.

II. MAGNON SCATTERING MODEL

The nonlinearity discussed in this article originates from the magnon scattering process. This process can be explained by the magnon dispersion [24], [25], shown in (1):

$$\omega_k = \gamma\sqrt{(H + \frac{A}{M_s}k^2 + 2M_s\tilde{T}_k^{xx})(H + \frac{A}{M_s}k^2 + 2M_s\tilde{T}_k^{yy})}\,, \tag{1}$$

where ω_k is the angular frequency of the magnon mode with wavevector k, k is the amplitude of the wavevector $\mathbf{k}$, H is the amplitude of applied field, A is the exchange constant, and M_s is the saturated magnetization. $2\tilde{T}_k^{ij}$ is the demagnetization tensor, in the dipole approximation, for a thin film [26].

For wavevectors parallel to applied field in Fig. 1, $\omega_{\mathbf{k}}$ first decreases versus $\mathbf{k}$ due to the magnetostatic interactions and forms a valley, then increases as the exchange interaction starts dominating at large wavevectors. The first Suhl instability happens at sufficiently high microwave power. For sufficiently small microwave pumping frequency ω_p and simultaneous adjustment of the applied field to match $\omega_{\mathbf{k}=0} = \omega_p$, the $\mathbf{k} = 0$ mode splits into $\mathbf{k} \neq 0$ magnons, which satisfy $\omega_{\mathbf{k}} = \omega_p/2$ with opposite wavevectors $\pm\mathbf{k}$. A well-defined frequency threshold for this process is expected, above which the dispersion lies above $\omega_p/2$ upon increasing the field to match $\omega_{\mathbf{k}=0}$ and ω_p.

III. METHODS

A. EXPERIMENT

The measurements are performed on a 3 μm thick YIG film that was grown by liquid phase epitaxy on a GGG substrate and obtained commercially [27]. Ferromagnetic resonance measurement confirms a magnetization $M_s = 146 \pm 1$ emu/cm^3 with a Gilbert damping parameter

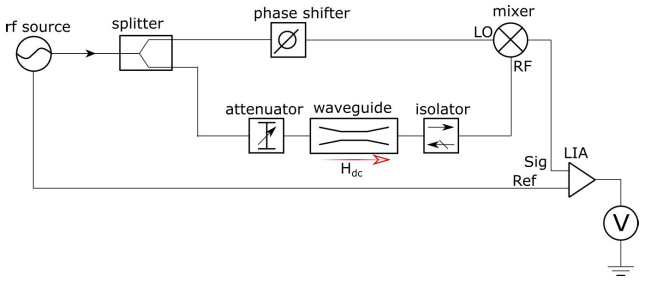

FIGURE 2. Schematic of homodyne spectrometer measurement set-up. A ∼ mm^2 cleaved piece of the sample was placed face-down over the center line of the coplanar waveguide with ground (similar to that used in Ref. [30]). The center line width of the CPW is 1.2 mm and the length is 25.4 mm.

$\alpha = (3.3\pm0.4) \times 10^{-4}$. An experimental investigation of the nonlinear magnon dynamics over a large dynamic range in power was achieved using homodyne spectrometer [28], as shown in Fig. 2. A microwave source, which is modulated at low frequency, is split into two paths of the spectrometer. For one path, a programmable attenuator controls the power going to the sample, which is placed on a coplanar waveguide. The transmitted signal from the sample is fed to the RF input of a balanced mixer. The Faraday isolator provides additional isolation. For the other path, a phase-shifted version of the microwave source passes into the local oscillator input of the mixer. The power in this path remains constant while the power to the sample in the other path is varied. Because the local oscillator input of the mixer is fixed, the mixer output is proportional to the amplitude of the transmitted signal from the sample, which is determined by the precessing magnetization [29], due to its inductive coupling to the waveguide. The signal is recorded by the lock-in amplifier.

B. SIMULATION

To understand the underlying physics of the nonlinearity, micromagnetic simulations were performed using the Landau-Lifshitz-Gilbert (LLG) equation [31]–[33]

$$\frac{d\hat{m}}{dt} = -\gamma\hat{m} \times (\vec{H}_{\text{eff}} + \vec{h}(t) + \vec{\eta}) + \alpha\hat{m} \times \frac{d\hat{m}}{dt}, \qquad (2)$$

where $\hat{m}$ is the unit vector of local magnetization of YIG, $\vec{h}(t)$ is the microwave field, $\vec{\eta}$ is the thermal fluctuation field at room temperature [34], [35], and $\vec{H}_{\text{eff}}$ is the effective field including the in-plane bias field $\vec{H}$, the spatially distributed magnetostatic field and the exchange field. α is the damping constant. The Cartesian coordinates are defined as follows: $+\hat{z}$ along the bias field direction, $+\hat{y}$ in-plane and perpendicular to the bias field, and $+\hat{x}$ along the out-of-plane direction, as shown in Fig. 3. In our perpendicular pumping configuration, $\vec{h}(t)$ is along $\hat{y}$. As the microwave pumping frequency f_p is ∼ GHz, the wavelength of the microwaves is ∼ cm. Compared to the measured YIG sample size of ∼ mm, the microwave field can be treated as a uniform field with a sine wave oscillating at ω_p. Due to the low coercivity of YIG, the sample's magnetization is saturated and aligned by $\vec{H}$. For a single crystalline structure, YIG on Gadolinium gallium garnet(GGG), we use the following parameters: gyromagnetic ratio $\gamma = 1.77 \times 10^7$ s^{-1}G^{-1}, $M_s = 146$ emu/cm^3, exchange constant A=3.5 $\times 10^{-7}$ erg/cm and time step Δt=50 fs. A home grown parallel computing code based on CUDA [19] is used to optimize the computational performance.

The system under study is 15 μm × 15 μm × 1.5 μm. The sample is discretized into cells with size 100 nm × 100 nm × 1.5 μm as a two-dimensional model. The reduction in film thickness for simulation is dictated by the need to capture all of the physics associated with the dipolar corrections to the dispersion relation (1) while achieving reasonable computational efficiency. A key fact is that the overall scale in wavevector is determined by the exchange and dipolar energies, which determine the location ($k \sim 10^5$ cm^{-1}) of the minimum in Fig. 1. At this scale, the function $[1 - \exp(-kD)]/kD$ characterizing the dipolar magnetostatic interactions is vanishing as $1/kD$. In this sense, the sample thickness $D = 3$ μm is already very large, and it suffices to choose a smaller thickness (1.5 μm) for the simulation. An alternative justification is provided by examining the critical magnons for the three-magnon process, i.e., those lying on the contour $\omega = \omega_p/2$, which assumes the butterfly shape in k-space, as shown in Fig. 4(a). Figure 9 of Appendix A shows an analogous calculation for a 3 μm thick YIG film. The similarity with Fig. 4(a) illustrates why using the thinner films for more efficient computation is justified, i.e., the thinner film retains all of the essential physics while reducing the number of cells required by a factor of 4, as the cell size in the transverse direction must scale with the thickness. This reduces the overall computation time by approximately a factor of 4log(4) relative to the value required if the full 3 μm thickness had been used.

We also have large latitude in the selection of a Gilbert damping parameter α in the simulation. As long as $\alpha \ll 1$, we remain in the weak damping regime, in which the only impact of changing α is to change the threshold power for non-linear behavior. We exploit this fact by selecting a relatively large $\alpha = 0.0014$ in our simulation for computational efficiency. This allows us to reduce the computational time necessary to reach the steady state by a factor of 4 relative to the experimental α (3.3×10^{-4}). This does not quantitatively (or qualitatively) affect the magnon dispersion, wavevectors, energies, etc.

It is also interesting to note that, for most wavevectors, the dispersion relation obtained from the micromagnetic simulations is consistent with the analytical prediction from (1), shown in Fig. 4(b). At larger wave-vectors, beyond the minimum, the simulation remains correct. The analytic model, however, begins to fail as the dipole approximation used to calculate the demagnetization tensor in (1) breaks down when $kD \geq 1$. To improve the analytic theory for magnons at larger wavevector, extra terms in the tensor, representing higher order multipoles would be required. These are, however, naturally captured in the simulation.

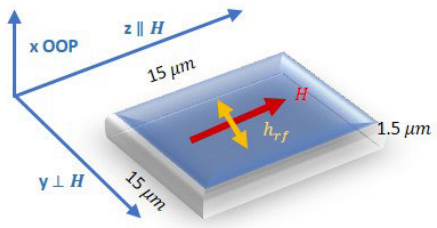

FIGURE 3. The YIG sample geometry with the field directions indicated.

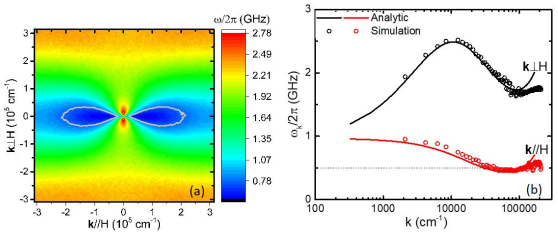

FIGURE 4. (a) Contour plot of simulated magnon dispersion in the two dimensional in-plane k space. The gray contour line shows magnon modes of constant angular frequency at $\omega_p/2$. (b) Analytical and simulated magnon dispersion for the magnon wave vector k ⊥ H and k // H.

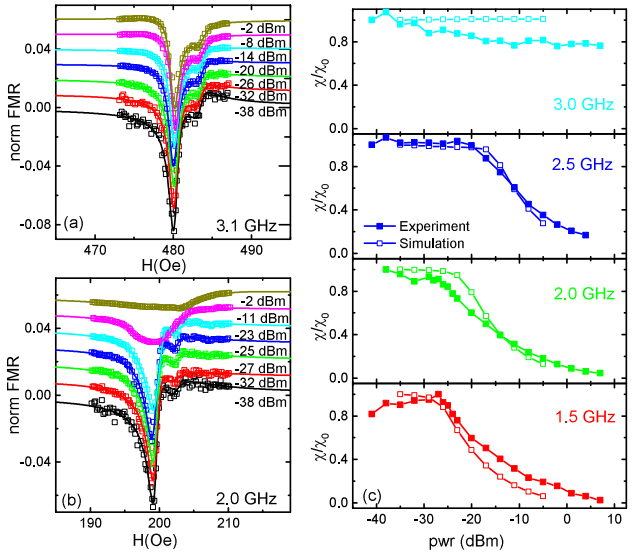

FIGURE 5. (a) the experimentally determined FMR dependence on microwave power at microwave frequency of 3.1 GHz. This frequency is above the nonlinear frequency threshold. (b) the experimentally determined FMR dependence on microwave power at microwave frequency of 2.0 GHz. This frequency is in the nonlinear frequency range. (c) The susceptibility at different powers normalized by the susceptibility at a very low power χ/χ_0, at varying microwave frequencies in both simulation and experiment. The horizontal axis for simulation has been shifted by 9 dB for all frequencies, to reflect the higher α usage in simulation.

IV. NONLINEARITY OBSERVATION IN SIMULATION AND EXPERIMENT

As a basis for comparing with simulation, ferromagnetic resonance (FMR) is measured as a function of field for a series of frequencies and excitation powers. As an example, the FMR signal normalized by transmitted voltage, at frequencies of 3.1 GHz and 2.0 GHz, is shown in Figs. 5 (a,b). At 3.1 GHz, the normalized FMR is nearly unchanged over three orders of microwave power amplitude. In contrast, the normalized FMR at 2.0 GHz, although nearly unchanged for powers up to −23 dBm, broadens significantly at higher powers, and is nearly suppressed above the excitation power of −2 dBm.

The experimental susceptibility χ is determined at each frequency f_P and power P by fitting the data to a two-phase Lorentzian function:

$$V_{dc}(H) = V_0 - \frac{B(\Delta H)^2}{4((H-H_0)^2 + (\Delta H)^2/4)} + \frac{F\,\Delta H(H-H_0)}{2((H-H_0)^2 + (\Delta H)^2/4)}, \quad (3)$$

where the fitting parameters are the resonant field H_0, linewidth ΔH, the quadrature amplitudes B and F, and the off-resonant transmitted amplitude V_0. The resonant amplitude $\sqrt{B^2+F^2}$ is the quadrature sum of the two components. In practice, the phase at each frequency is adjusted to maximize the symmetric component at the lowest power. To obtain the susceptibility, we normalize by the voltage V_0, which is proportional to the microwave amplitude, and then divide by f_p, which accounts for the fact that the electromagnetic field for a given magnetization precession amplitude is proportional to frequency [29]. Hence,

$$\chi \propto \frac{\sqrt{B^2+F^2}}{f_p V_0}. \quad (4)$$

The experimental and simulated susceptibilities as a function of microwave power are compared in Fig. 5(c) for several different microwave frequencies. We find that at and above 3 GHz, the response is essentially linear over the entire range of excitation power. At lower frequencies however, a well-defined power threshold is observed, above which the maximum susceptibility decreases due to the onset of three magnon scattering. At the experimental thickness of 3.0 μm, the maximum frequency f_{th} at which the magnon-magnon process can occur is predicted by (1) to be 2.96 GHz. This is the highest frequency for which a minimum in the dispersion relation (see Fig. 1) occurs at frequency less than or equal to $f_{th}/2$. In experiment, we find that the power threshold disappears above 3.0 ± 0.1 GHz, in good agreement with the predicted value. The power threshold observed for frequencies below f_{th} is the Suhl instability originally found in YIG spheres [7]. The power threshold in Fig. 5(c) is commonly used to characterize the performance of nonlinear microwave/RF applications, such as frequency selective limiters and signal to noise enhancers [19]–[21]: it identifies the minimum power that will experience excess attenuation. The power dependent susceptibility in Fig. 5(c) determines the insertion loss, which is another common factor used to characterize the performance: it determines the attenuation level for over-threshold inputs. This nonlinear feature allows the material to attenuate undesirable inputs, while sustaining the useful signal [36].

Insight into the connection between the susceptibility and magnon-magnon scattering is revealed by the magnon

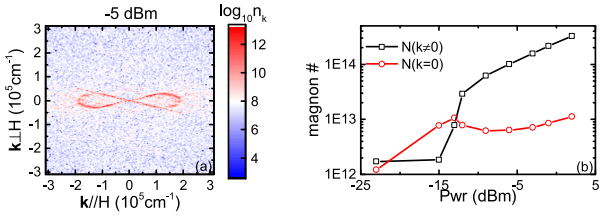

FIGURE 6. (a) Contour plot of the magnon number $n_{\mathbf{k}}$ at a microwave power of −5 dBm, which is above the threshold frequency for three-magnon scattering. The magnon number $n_{\mathbf{k}}$ is obtained at the steady state. The microwave pump frequency f_p is 1.5 GHz. The generated $\mathbf{k} \neq 0$ magnons are degenerate with frequency of $f_p/2$=0.75 GHz. (b) The number of magnon states versus the microwave power. The black data are the integrated magnon number $N(\mathbf{k} \neq 0)$ of non-uniform magnons, as integrated over points in k-space satisfying $\omega_{\mathbf{k}} = \omega_p/2$. The red data represent the uniform magnon number $N(\mathbf{k} = 0)$.

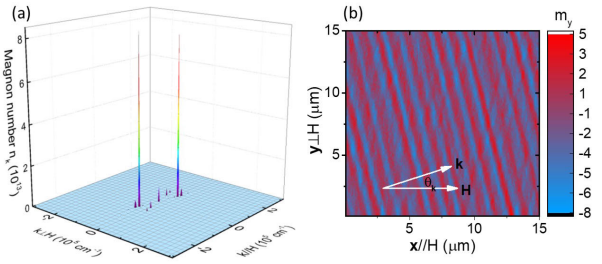

FIGURE 7. (a) The 3D plot of magnon number versus in-plane k-space at 1.0GHz. (b) Spatial contour of magnetization component m_y parallel with the microwave field at 1.0 GHz. Both figures are obtained at the steady state.

TABLE 1. Properties of Excited Magnon Modes at Varying Microwave Frequencies. The Modes are Always Excited in Pairs at Equal and Opposite Wave-Vectors. Note That θ_k is the Angle Between the Magnon Wave-Vector and the Applied Field Direction.

microwave frequency ω_p (GHz)	magnon wavevector $\mathbf{k}$ (cm^{-1})	wavelength λ (nm)	propagation angle θ_k (deg)
1	$(4.83 \times 10^4, 1.13 \times 10^4)$	1267	13.2
1.5	$(7.42 \times 10^4, 2.06 \times 10^4)$	816	15.5
2.0	$(7.81 \times 10^4, 1.82 \times 10^4)$	783	13.1
2.5	$(7.81 \times 10^4, 1.13 \times 10^4)$	796	8.3

number. Appendix B describes a rigorous method to precisely calculate the number of elliptical magnons (the appropriate eigenmodes for the thin film geometry) as a function of wave-vector. The magnon number $n_{\mathbf{k}}$ is calculated from the spatial and temporal Fourier transform of the simulated magnetization. For a spatially uniform microwave excitation field in the linear power regime, $N(\mathbf{k})$ is therefore a delta function at $\mathbf{k} = 0$ and $\omega = \omega_p$. As the power increases above the three-magnon threshold, magnon scattering is activated, and a large number of $\mathbf{k} \neq 0$ magnons are generated at frequency $\omega_p/2$. Fig. 6(a) shows the magnon number in steady-state for an excitation frequency $f_p = 1.5$ GHz at a power (-5 dBm) that is above threshold. The magnons generated by three-magnon scattering occupy a curve in k-space satisfying $\omega_{\mathbf{k}} = \omega_p/2$. This corresponds to the contour shown in the dispersion relation of Fig. 4(a). We can find the total number of magnons generated at non-zero wave-vector by integrating $N(\mathbf{k})$ along this contour curve. At low microwave power, only $\mathbf{k} = 0$ magnons are generated, $N(\mathbf{k} = 0)$ increases linearly with power, and $N(\mathbf{k} \neq 0)$ is negligible. In this regime, all of the energy is stored in the uniform mode. Above the threshold frequency, $N(\mathbf{k} \neq 0)$ increases from the background thermal value, while $N(\mathbf{k} = 0)$ is approximately constant, as shown in Fig. 6(b). The sharp decrease in the susceptibility in Fig. 5(c) corresponds to the redistribution of magnons from $\mathbf{k} = 0$ to $\mathbf{k} \neq 0$.

A second feature observed in the data and simulation is that the power threshold P_{th} for the onset of the instability increases with increasing frequency, as shown in Fig. 5(c). At the lowest f_p, 2.0 GHz, $P_{th} = -25$ dBm, and it increases to -14 dBm at $f_p = 2.8$ GHz. P_{th} can be converted to the microwave field threshold h_{th}, using (5),

$$h_{th} = \sqrt{\frac{2P}{R_{load}}}/d_{CPW}\,, \tag{5}$$

where R_{load} is the load resistance (50 Ω) and d_{CPW} is the coplanar waveguide width. Given the simulation parameters, h_{th} at 2.0 GHz is 7.1×10^{-4} Oe while at 2.9 GHz, $h_{th} = 2 \times 10^{-3}$ Oe. The estimated precession cone angle is $< 0.5°$. The nonlinearity therefore occurs at a very low microwave field. Although the three-magnon process, including the onset of magnon generation at $\omega_p/2$, has been observed directly by Brillouin light scattering [18], the broadband measurements here show quantitative agreement with theory over a wide dynamic range of frequency and power. Unfortunately, it is impossible to use the stripline technique to observe the modes at non-zero wavevector.

V. MAGNON PAIR AT THE POWER THRESHOLD

Focusing on the microwave frequencies in the nonlinear region, we find that just above the power threshold, magnon pairs are generated as shown in Fig. 7(a). Because these correspond to opposite wave-vectors, their superposition is approximately a standing wave in space, as illustrated by the plot of the in-plane precession amplitude (m_y) in Fig. 7(b). It is perhaps surprising that the excited modes are focused over such a small range of propagation angles, which is clearly different from the direction of the applied magnetic field. In practice, there are two sets of magnon pairs that can be excited, so that up to four peaks in the magnon density can be observed in k-space. The wave-vectors corresponding to the peaks at several different frequencies are given in Table 1. This ability to precisely select a particular magnon pair is important for spintronic devices, where better control of magnon production means better conveyance of information, and thus better processing speeds and capacity. It also may benefit the accuracy and the efficiency of parametrized nonlinear circuit models [37], [38], where simple models of scattering are used to approximate device functions. The magnons are approximated by equivalent circuit units, such as resistances, inductors and capacitors. Knowledge of the contributing magnons helps identify the most significant circuit

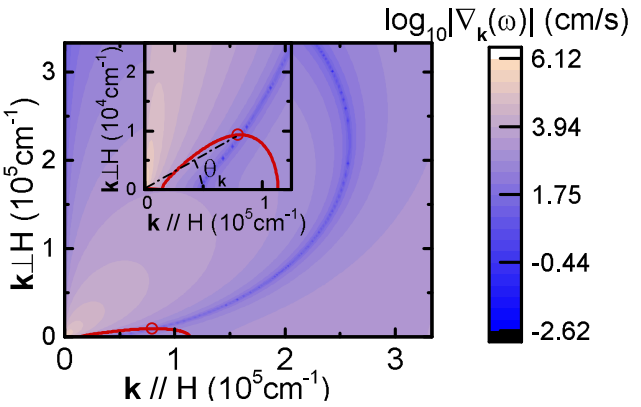

FIGURE 8. Contour plot of group velocity in the two dimensional k space, produced as described in Appendix C. The microwave frequency is 2.5 GHz. The red curve represents the modes at the energy level of $f_p/2$, obtained from magnon dispersion. The deep-blue band represents the minimum group velocity. The intersection point (marked as a red dot) of red line and deep-blue band indicates the unique magnon mode, that fulfills the energy of $f_p/2$ and the minimum group velocity. This mode has a propagation angle θ_k as 6.7 deg, consistent with our simulation result in Table 1. The inset is a magnified image of the region at small wave vectors.

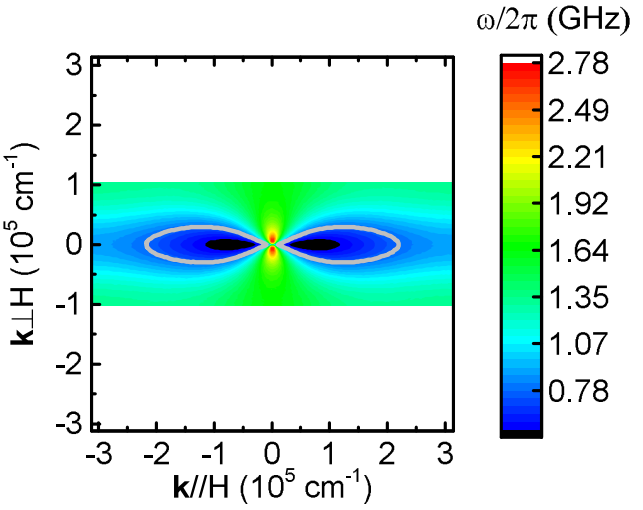

FIGURE 9. The magnon dispersion at the thickness of 3.0 um, obtained from simulation. The grey contour line show magnon modes of angular frequency at $\omega_p/2$.

units and, thus, should reduce the number of circuit units needed.

As is evident from Fig. 7(b), the wavelengths of the magnons excited in the three-magnon process are $\sim$ 1000 nm, which corresponds to the dipole-exchange interaction region [11], [12] (around the minimum) of the dispersion relation. The angle of propagation is determined by the need to satisfy energy conservation while simultaneously considering where the magnon density of states is largest in **k**-space. The density of states is proportional to $|\nabla_{\mathbf{k}}(\omega)|^{-1}$, which is the inverse of magnitude of the group velocity. The propagation angle for scattered magnons is therefore determined by the points at which the density of states diverges along the contour $\omega = \omega_p/2$. The details of this calculation are provided in Appendix C, and an example for the case $\omega_p = 2.5$ GHz is shown in Fig. 8. The angle θ_k of the propagating mode is theoretically predicted as $\sim$ 10 degrees, consistent with our simulated result in Table 1. In principle, this focusing of magnons in **k**-space should be observable by Brillouin light scattering (BLS), and indeed there is some evidence for this in the work of Ordonez-Romero *et al.* [18], although the high microwave power required excites magnons over a larger fraction of the $\omega = \omega_p/2$ contour. The standing wave character and high directionality of this mode of excitation could be useful technologically for confining energy to particular regions of a sample as well as conversion to other degrees of freedom, such as phonons [12]. The combination of parametric pumping and spatial selectivity might also be used as a spin wave filter.

VI. CONCLUSION

By combining analytical theory with our simulated results, we have established a rigorous technique of calculating magnon numbers at any wave-vector for magnetic thin films under microwave pumping. We emphasize that this approach is applicable to a wide range of pumping conditions, although we have focused in this article on the three-magnon process. We have demonstrated that the prediction for the frequency and power dependence, including the expected threshold behavior, is consistent with experiment. We have also shown that near threshold, the primary magnons excited are those with the minimum group velocity while simultaneously satisfying energy conservation. This allows more distinct scattering states to be available within thermal broadening and limits energy transfer (radiation) between localities, thus promoting further scattering. This localization has important implications for the technology of nonlinear devices and for simplified device modeling (because boundary conditions are less important). More generally, the approach can be applied to a variety of spin wave devices where there is a need to select excitation conditions to produce magnons with a specific frequency and wave-vector.

APPENDIX A
THICKNESS DEPENDENCE OF MAGNON DISPERSION

The simulated dispersion for a 3 μm film under external field of 148 Oe (the same as used for the simulation shown in Fig. 4(a)) is shown in Fig. 9. The important frequency at this field is $f_p/2 = 0.75$ GHz, which corresponds to the gray contour in Fig. 9. Its similarity to the dispersion contour at the same frequency shown in Fig. 4(a) strongly suggests that 1.5 μm yields very similar results to the 3μm experimental thickness.

APPENDIX B
TECHNIQUE FOR CALCULATING MAGNON NUMBER

Due to the precessional nature of the magnetization, it is convenient to define the following variables: $m^+ = m_x + im_y = \sum a_{\mathbf{k}} e^{i\mathbf{kr}}$, $m^- = m_x - im_y = \sum a_{\mathbf{k}}^- e^{-i\mathbf{kr}}$, where m_x, m_y, and m_z are the normalized magnetizations [24], [39],

where the x, y, and z coordinates are shown in Fig. 3. The ordinary magnon operaturs $a_{\mathbf{k}}$ and $a_{\mathbf{k}}^{-}$ represent the counter-clockwise/clockwise polarization respectively in $\mathbf{k}$ space. The Landau-Lifshitz equation can be rewritten in this representation as:

$$\begin{pmatrix} \dot{a}_{\mathbf{k}} \\ \dot{a}^*_{-\mathbf{k}} \end{pmatrix} = \begin{pmatrix} iA_{\mathbf{k}} & iB_{\mathbf{k}} \\ -iB^*_{\mathbf{k}} & -iA_{\mathbf{k}} \end{pmatrix} \begin{pmatrix} a_{\mathbf{k}} \\ a^*_{-\mathbf{k}} \end{pmatrix}; \tag{6}$$

$$A_{\mathbf{k}} = \omega_H + \omega_{ex} l^2 k^2 + \omega_M (\tilde{T}^{xx}_{\mathbf{k}} + \tilde{T}^{yy}_{\mathbf{k}}); \tag{7}$$

$$B_{\mathbf{k}} = \omega_M (\tilde{T}^{xx}_{\mathbf{k}} - \tilde{T}^{yy}_{\mathbf{k}}), \tag{8}$$

where $k^2 = k_y^2 + k_z^2$, γ is the gyromagnetic ratio, $\omega_H = \gamma H$ is the precession angular frequency at applied field amplitude H, ω_{ex} is the angular frequency of the exchange field, and $\omega_M = \gamma M_s$ is the magnetization angular frequency determined by the saturation magnetization M_s. The demagnetization tensor $2\tilde{T}^{ij}_{\mathbf{k}}$ for a thin film [26] with thickness D, k_x taken to be zero, and i, j are x, y, z, is given by:

$$2\tilde{T}^{ij}_{\mathbf{k}} = \begin{pmatrix} 4\pi(1 - G(kD)) & 0 & 0 \\ 0 & 4\pi G(kD)\dfrac{k_y^2}{k^2} & 4\pi G(kD)\dfrac{k_y k_z}{k^2} \\ 0 & 4\pi G(kD)\dfrac{k_y k_z}{k^2} & 4\pi G(kD)\dfrac{k_z^2}{k^2} \end{pmatrix}; \tag{9}$$

$$G(x) = 1 - \frac{1 - \exp(-x)}{x}. \tag{10}$$

Introducing the Holstein-Primakoff transformation [40] to transform circular magnons $a_{\mathbf{k}}$ and $a^*_{-\mathbf{k}}$ to elliptical magnons $b_{\mathbf{k}}$ and $b^*_{-\mathbf{k}}$, in order to eliminate the non-diagonal elements in (6):

$$\begin{pmatrix} b_{\mathbf{k}} \\ b^*_{-\mathbf{k}} \end{pmatrix} = \begin{pmatrix} \lambda_{\mathbf{k}} & \mu_{\mathbf{k}} \\ \mu^*_{\mathbf{k}} & \lambda_{\mathbf{k}} \end{pmatrix} \begin{pmatrix} a_{\mathbf{k}} \\ a^*_{-\mathbf{k}} \end{pmatrix}. \tag{11}$$

The transformation coefficient in $\lambda_{\mathbf{k}}$ and $\mu_{\mathbf{k}}$ in (11) is written as:

$$\lambda_{\mathbf{k}} = \cosh\left(\frac{\operatorname{arctanh}(\frac{|B_{\mathbf{k}}|}{A_{\mathbf{k}}})}{2}\right); \tag{12}$$

$$\mu_{\mathbf{k}} = \sinh\left(\frac{\operatorname{arctanh}(\frac{|B_{\mathbf{k}}|}{A_{\mathbf{k}}})}{2}\right), \tag{13}$$

where $\lambda_{\mathbf{k}}$ and $\mu_{\mathbf{k}}$ indicate the mixing of circular magnons, caused by thin film geometry. Fig.10 shows our calculated values of $\lambda_{\mathbf{k}}$ and $\mu_{\mathbf{k}}$ in the case of YIG.

The elliptical magnon number $n_{\mathbf{k}}$ is then:

$$n_{\mathbf{k}} = b^*_{\mathbf{k}} b_{\mathbf{k}}, \tag{14}$$

Using a hybrid method of Holstein Primakoff transformation and Fourier transforms of the simulated magnetization in both time and space, we can therefore calculate the magnon number rigorously.

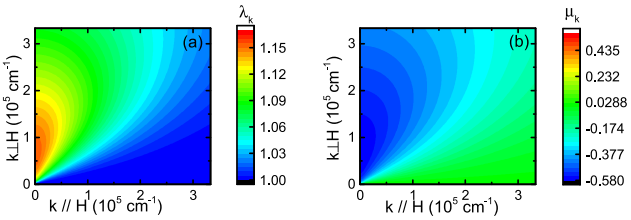

FIGURE 10. The transformation parameters $\lambda_{\mathbf{k}}$(a) and $\mu_{\mathbf{k}}$(b) in k space. The microwave pump frequency is 1.5 GHz.

APPENDIX C
GROUP VELOCITY IN A THIN FILM

The dispersion relation $\omega_{\mathbf{k}} = \sqrt{A_{\mathbf{k}}^2 - B_{\mathbf{k}}^2}$ can be obtained from (6) in Appendix B. The definition of the group velocity is $\mathbf{v_k} = \nabla_{\mathbf{k}}\omega_{\mathbf{k}}$. Consequently, the velocity components v_y (perpendicular to the field direction) and v_z (along the field direction) are:

$$v_y = \frac{\partial \omega_{\mathbf{k}}}{\partial k_y} \tag{15}$$

$$= \frac{A_{\mathbf{k}} \frac{\partial A_{\mathbf{k}}}{\partial k_y} - B_{\mathbf{k}} \frac{\partial B_{\mathbf{k}}}{\partial k_y}}{\sqrt{A_{\mathbf{k}}^2 - B_{\mathbf{k}}^2}}; \tag{16}$$

$$v_z = \frac{\partial \omega_{\mathbf{k}}}{\partial k_z} \tag{17}$$

$$= \frac{A_{\mathbf{k}} \frac{\partial A_{\mathbf{k}}}{\partial k_z} - B_{\mathbf{k}} \frac{\partial B_{\mathbf{k}}}{\partial k_z}}{\sqrt{A_{\mathbf{k}}^2 - B_{\mathbf{k}}^2}}. \tag{18}$$

Using (7) and (8) in Appendix B, we obtain:

$$\frac{\partial A_{\mathbf{k}}}{\partial k_y} = 2\omega_{ex} l^2 k_y + 2\pi\omega_M \frac{2 k_y k_z^2}{k^4}(3\, G(kD) - 1 + e^{-kD}); \tag{19}$$

$$\frac{\partial A_{\mathbf{k}}}{\partial k_z} = 2\omega_{ex} l^2 k_z - \frac{2\pi\omega_M}{k^4}(2 k_y^2 k_z G(kD) + (1 - G(kD) - e^{-kD}) k_z^3); \tag{20}$$

$$\frac{\partial B_{\mathbf{k}}}{\partial k_y} = -2\pi\omega_M \left(\left(1 - G(kD) - e^{-kD}\right)\frac{k_y}{k^2}\left(1 + \frac{k_y^2}{k^2}\right)\right) - 2\pi\omega_M G(kD)\frac{2 k_y k_z^2}{k^4}; \tag{21}$$

$$\frac{\partial B_{\mathbf{k}}}{\partial k_z} = -2\pi\omega_M \left(\left(1 - G(kD) - e^{-kD}\right)\frac{k_z}{k^2}\left(1 + \frac{k_y^2}{k^2}\right)\right) + 2\pi\omega_M G(kD)\frac{2k_y^2 k_z}{k^4}. \tag{22}$$

ACKNOWLEDGMENT

The authors acknowledge XSEDE P100 and K80 GPU nodes at XStream, Comet and Bridges through allocation TG-ENG180002 for support of the initial computational work. They would also like to thank the Minnesota Supercomputing Institute (MSI), University of Minnesota, for providing

resources that contributed to the research results reported within this article. They would like to thank Benjamin Lynch, Brent Swartz and David Porter (MSI) for fruitful discussions on parallel computation, Anand Gopinath and Wen Zhou for valuable suggestions on microwave devices, and Jackie Yao, Helen Cui and Ethan Wang for valuable discussions on nonlinear microwave engineering applications.

REFERENCES

[1] J. Grollier, D. Querlioz, and M. D. Stiles, "Spintronic nanodevices for bioinspired computing," *Proc. IEEE*, vol. 104, no. 10, pp. 2024–2039, Oct. 2016.

[2] S. Petit-Watelot, J.-V. Kim, A. Ruotolo, R. M. Otxoa, K. Bouzehouane, J. Grollier, A. Vansteenkiste, B. Van de Wiele, V. Cros, and T. Devolder, "Commensurability and chaos in magnetic vortex oscillations," *Nature Phys.*, vol. 8, no. 9, pp. 682–687, 2012.

[3] J. W. Fleischer, M. Segev, N. K. Efremidis, and D. N. Christodoulides, "Observation of two-dimensional discrete solitons in optically induced nonlinear photonic lattices," *Nature*, vol. 422, no. 6928, pp. 147–150, 2003.

[4] G. Wiese, P. Kabos, and C. E. Patton, "Subsidiary absorption spin wave instability processes in yttrium iron garnet thin films, critical modes, and the 'kink' effect," *J. Appl. Phys.*, vol. 74, no. 2, pp. 1218–1228, 1993.

[5] P. Pirro, T. Sebastian, T. Brächer, A. A. Serga, T. Kubota, H. Naganuma, M. Oogane, Y. Ando, and B. Hillebrands, "Non-Gilbert-damping mechanism in a ferromagnetic heusler compound probed by nonlinear spin dynamics," *Phys. Rev. Lett.*, vol. 113, no. 22, Nov. 2014, Art. no. 227601.

[6] P. Krivosik and C. E. Patton, "Hamiltonian formulation of nonlinear spin-wave dynamics: Theory and applications," *Phys. Rev. B, Condens. Matter*, vol. 82, no. 18, Nov. 2010, Art. no. 184428.

[7] H. Suhl, "The theory of ferromagnetic resonance at high signal powers," *J. Phys. Chem. Solids*, vol. 1, no. 4, pp. 209–227, Jan. 1957.

[8] K. Schultheiss, R. Verba, F. Wehrmann, K. Wagner, L. Körber, T. Hula, T. Hache, A. Kákay, A. A. Awad, V. Tiberkevich, A. N. Slavin, J. Fassbender, and H. Schultheiss, "Excitation of whispering gallery magnons in a magnetic vortex," *Phys. Rev. Lett.*, vol. 122, no. 9, Mar. 2019, Art. no. 097202.

[9] Z. Zhang, M. Vogel, J. Holanda, J. Ding, M. B. Jungfleisch, Y. Li, J. E. Pearson, R. Divan, W. Zhang, A. Hoffmann, Y. Nie, and V. Novosad, "Controlled interconversion of quantized spin wave modes via local magnetic fields," *Phys. Rev. B, Condens. Matter*, vol. 100, no. 1, Jul. 2019, Art. no. 014429.

[10] X. Zhang, C.-L. Zou, L. Jiang, and H. X. Tang, "Strongly coupled magnons and cavity microwave photons," *Phys. Rev. Lett.*, vol. 113, no. 15, Oct. 2014, Art. no. 156401.

[11] H. G. Bauer, P. Majchrak, T. Kachel, C. H. Back, and G. Woltersdorf, "Nonlinear spin-wave excitations at low magnetic bias fields," *Nature Commun.*, vol. 6, no. 1, p. 8274, Nov. 2015.

[12] H. Hayashi and K. Ando, "Spin pumping driven by magnon polarons," *Phys. Rev. Lett.*, vol. 121, no. 23, Dec. 2018, Art. no. 237202.

[13] C. L. Chang, A. M. Lomonosov, J. Janusonis, V. S. Vlasov, V. V. Temnov, and R. I. Tobey, "Parametric frequency mixing in a magnetoelastically driven linear ferromagnetic-resonance oscillator," *Phys. Rev. B, Condens. Matter*, vol. 95, no. 6, Feb. 2017, Art. no. 060409.

[14] H. Kurebayashi, O. Dzyapko, V. E. Demidov, D. Fang, A. J. Ferguson, and S. O. Demokritov, "Spin pumping by parametrically excited short-wavelength spin waves," *Appl. Phys. Lett.*, vol. 99, no. 16, Oct. 2011, Art. no. 162502.

[15] F. Guo, L. M. Belova, and R. D. Mcmichael, "Nonlinear ferromagnetic resonance shift in submicron permalloy ellipses," *Phys. Rev. B, Condens. Matter*, vol. 91, no. 6, Feb. 2015, Art. no. 064426.

[16] D. D. Stancil and A. Prabhakar, *Spin Waves Theory and Applications*. New York, NY, USA: Springer.

[17] H. J. J. Liu, G. A. Riley, C. L. Ordóñez-Romero, B. A. Kalinikos, and K. S. Buchanan, "Time-resolved study of nonlinear three-magnon processes in yttrium iron garnet films," *Phys. Rev. B, Condens. Matter*, vol. 99, no. 2, Jan. 2019, Art. no. 024429.

[18] C. L. Ordóñez-Romero, B. A. Kalinikos, P. Krivosik, W. Tong, P. Kabos, and C. E. Patton, "Three-magnon splitting and confluence processes for spin-wave excitations in yttrium iron garnet films: Wave vector selective Brillouin light scattering measurements and analysis," *Phys. Rev. B, Condens. Matter*, vol. 79, no. 14, Apr. 2009, Art. no. 144428.

[19] A. Venugopal, T. Qu, and R. H. Victora, "Nonlinear parallel-pumped FMR: Three and four Magnon processes," *IEEE Trans. Microw. Theory Techn.*, vol. 68, no. 2, pp. 602–610, Feb. 2020.

[20] J. D. Adam and S. N. Stitzer, "Frequency selective limiters for high dynamic range microwave receivers," *IEEE Trans. Microw. Theory Techn.*, vol. 41, no. 12, pp. 2227–2231, Dec. 1993.

[21] J. D. Adam and F. Winter, "Magnetostatic wave frequency selective limiters," *IEEE Trans. Magn.*, vol. 49, no. 3, pp. 956–962, Mar. 2013.

[22] G. Csaba, Á. Papp, and W. Porod, "Perspectives of using spin waves for computing and signal processing," *Phys. Lett. A*, vol. 381, no. 17, pp. 1471–1476, May 2017.

[23] S. Rumyantsev, M. Balinskiy, F. Kargar, A. Khitun, and A. A. Balandin, "The discrete noise of magnons," *Appl. Phys. Lett.*, vol. 114, no. 9, Mar. 2019, Art. no. 090601.

[24] B. Kalinikos and A. Slavin, "Theory of dipole-exchange spin wave spectrum for ferromagnetic films with mixed exchange boundary conditions," *J. Phys. C, Solid State Phys.*, vol. 19, no. 35, p. 7013, 1986.

[25] E. Iacocca and O. Heinonen, "Topologically nontrivial magnon bands in artificial square spin ices with dzyaloshinskii-moriya interaction," *Phys. Rev. A, Gen. Phys.*, vol. 8, no. 3, Sep. 2017, Art. no. 034015.

[26] A. Y. Dobin and R. H. Victora, "Intrinsic nonlinear ferromagnetic relaxation in thin metallic films," *Phys. Rev. Lett.*, vol. 90, no. 16, Apr. 2003, Art. no. 167203.

[27] *MTI Corporation*. Accessed: Mar. 1, 2020. [Online]. Available: https://www.mtixtl.com/YIG-GGG-c101005.aspx

[28] S. Tamaru, K. Yakushiji, A. Fukushima, S. Yuasa, and H. Kubota, "Ultrahigh sensitivity ferromagnetic resonance measurement based on microwave interferometer," *IEEE Magn. Lett.*, vol. 5, pp. 1–4, 2014.

[29] M. Kostylev, "Coupling of microwave magnetic dynamics in thin ferromagnetic films to stripline transducers in the geometry of the broadband stripline ferromagnetic resonance," *J. Appl. Phys.*, vol. 119, no. 1, Jan. 2016, Art. no. 013901.

[30] W. K. Peria, T. A. Peterson, A. P. McFadden, T. Qu, C. Liu, C. J. Palmstrøm, and P. A. Crowell, "Interplay of large two-magnon ferromagnetic resonance linewidths and low Gilbert damping in Heusler thin films," *Phys. Rev. B, Condens. Matter*, vol. 101, Apr. 2020, Art. no. 134430.

[31] J. Towns, T. Cockerill, M. Dahan, I. Foster, K. Gaither, A. Grimshaw, V. Hazlewood, S. Lathrop, D. Lifka, G. D. Peterson, R. Roskies, J. R. Scott, and N. Wilkins-Diehr, "XSEDE: Accelerating scientific discovery," *Comput. Sci. Eng.*, vol. 16, no. 5, pp. 62–74, Sep. 2014.

[32] N. A. Natekar, W.-H. Hsu, and R. H. Victora, "Calculated dependence of FePt damping on external field magnitude and direction," *AIP Adv.*, vol. 7, no. 5, May 2017, Art. no. 056004.

[33] M. J. Donahue, "Parallelizing a micromagnetic program for use on multiprocessor shared memory computers," *IEEE Trans. Magn.*, vol. 45, no. 10, pp. 3923–3925, Oct. 2009.

[34] W. F. Brown, "Thermal fluctuations of a single-domain particle," *Phys. Rev.*, vol. 130, no. 5, pp. 1677–1686, Jun. 1963.

[35] Z. Liu, P.-W. Huang, G. Ju, and R. H. Victora, "Thermal switching probability distribution of L10 FePt for heat assisted magnetic recording," *Appl. Phys. Lett.*, vol. 110, no. 18, May 2017, Art. no. 182405.

[36] A. Venugopal, T. Qu, and R. H. Victora, "Manipulation of nonlinear magnon effects using a secondary microwave frequency," *Appl. Phys. Lett.*, vol. 117, no. 15, Oct. 2020, Art. no. 152404.

[37] H. Cui, Z. Yao, and Y. E. Wang, "Coupling electromagnetic waves to spin waves: A physics-based nonlinear circuit model for frequency-selective limiters," *IEEE Trans. Microw. Theory Techn.*, vol. 67, no. 8, pp. 3221–3229, Aug. 2019.

[38] J. D. Adam, S. N. Stitzer, and R. M. Young, "UHF frequency selective limiters," in *IEEE MTT-S Int. Microw. Symp. Dig.*, vol. 2, May 2001, pp. 1173–1174.

[39] R. W. Damon and J. R. Eshbach, "Magnetostatic modes of a ferromagnet slab," *J. Phys. Chem. Solids*, vol. 19, nos. 3–4, pp. 308–320, May 1961.

[40] M. Sparks, *Ferromagnetic-Relaxation Theory*. New York, NY, USA: McGraw-Hill, 1964.

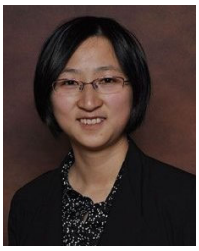

TAO QU (Member, IEEE) received the B.S. degree in physics from the University of Technology and Science of China, in 2009, the M.S degree in electrical engineering and the Ph.D. degree in physics from the University of Minnesota, in 2013 and 2017, respectively. She currently holds a postdoctoral position with the Department of Electrical and Computer Engineering, University of Minnesota. Her current research interests include magnetics, focusing on the fundamental theory, simulation, and microwave measurement of magnetization materials and dynamics, and their applications in spintronics and microwave/RF engineering.

ANEESH VENUGOPAL (Graduate Student Member, IEEE) received the B.Tech. degree in electronics and communication engineering from the Cochin University of Science and Technology, in 2010, and the M.S. degree in electrical engineering (specializing in solid state) from the University of Michigan, in 2015. He is currently pursuing the Ph.D. degree with the Department of Electrical and Computer Science, University of Minnesota. Until 2013, he was with Tata Consultancy Services, Chennai, India. His current research interest includes magnetics, focusing on magnetization dynamics with possible applications in magnonics and microwave devices.

JAMES M. ETHERIDGE received the B.Sc. degree in physics from The Ohio State University, in 2017. He is currently a Graduate Student with the Department of Physics, University of Minnesota. His research interest includes the interfacial properties of iron thin films grown on semiconductor substrates.

WILLIAM K. PERIA received the B.S. degrees in physics and mathematics from the University of Minnesota, in 2017, where he is currently pursuing the Ph.D. degree. His research interest includes the experimental studies of magnetization dynamics in a wide variety of magnetic thin film systems using ferromagnetic resonance and structural characterization techniques.

KARTHIK SRINIVASAN (Graduate Student Member, IEEE) received the bachelor's degree in electronics and communication engineering from Anna University, Chennai, India, in 2016, and the master's degree in electrical engineering from the University of Minnesota, MN, USA, in 2019, where he is currently pursuing the Ph.D. degree with the Department of Electrical and Computer Engineering. His research interests include the growth and characterization of magneto-optical materials and ferrimagnetic insulators for photonic and magnonic applications.

BETHANIE J. H. STADLER (Senior Member, IEEE) received the bachelor's degree from Case Western Reserve University and the Ph.D. degree from the Massachusetts Institute of Technology. She is currently a Professor and the Associate Head of electrical and computer engineering with the University of Minnesota. Her research interests include the fabrication and applications of highly gyrotropic garnet films and magnetic nanowires. She is a Fellow of the Materials Research Society. She served as a Distinguished Lecturer for the IEEE Magnetic Society.

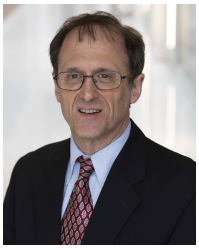

PAUL A. CROWELL (Member, IEEE) received the Ph.D. degree in low-temperature physics from Cornell University, in 1994. He was a Postdoctoral Associate with CNRS, Grenoble, and also with the University of California at Santa Barbara. In 1997, he joined the Faculty of the University of Minnesota. He is currently a Professor of physics and the Head of the School of Physics and Astronomy. Hi research interests include spin dynamics in ferromagnets on sub-nanosecond time scales and spin transport in hybrid ferromagnet-semiconductor and ferromagnet/normal metal systems. He is a Fellow of the American Physical Society.

R. H. VICTORA (Fellow, IEEE) received the B.S. degree from the Massachusetts Institute of Technology (MIT), in 1980, and the Ph.D. degree in physics from UC Berkeley, in 1985. In 1985, he joined Kodak Research Laboratories, where he was with the University of Minnesota until 1998. He has been serving as the Head for the Department of Electrical and Computer Engineering since 2015. His research interest includes the theory and simulation of magnetic materials.

Dr. Victora is a Fellow of the American Physical Society. He is best known for his work on recording media, for which he has received several awards including the Achievement Award of the Institute of Electrical and Electronics Engineers (IEEE) Magnetics Society. He served as the General Chair for the 50th Conference on Magnetism and Magnetic Materials and also as the President for the IEEE Magnetics Society.